Anisotropic dynamics of charge carriers in graphene

Géza I. Márk,[1,2,*] Péter Vancsó,[1,2] Chanyong Hwang,[2,3] Philippe Lambin,[4] and László P. Biró[1,2]

[1]*Research Institute for Technical Physics and Materials Science, H-1525 Budapest, P.O. Box 49, Hungary*

[2]*Korean-Hungarian Joint Laboratory for Nanosciences, H-1525 Budapest, P.O. Box 49, Hungary*

[3]*Center for Advanced Instrumentation, Division of Industrial Metrology, Korea Research Institute of Standards and Science, Yuseong, Daejeon 305-340, Republic of Korea*

[4]*Department of Physics of Matter and Radiations, University of Namur FUNDP, 61, Rue de Bruxelles, B-5000 Namur, Belgium*

(Received 20 November 2011; revised manuscript received 28 January 2012; published 30 March 2012)

Computer simulation by numerically solving the time-dependent Schrödinger equation was used to investigate the spreading of electronic wave packets on the graphene surface injected from a local probe. The simulations show a highly anisotropic in-plane dynamics following a 60° angular periodicity even near the Fermi energy. The wave packet first tunnels onto the small graphene clusters below the tip and the electronic states of these clusters govern the further spreading of the electron on the graphene surface. It was found that in the vicinity of the injection point the molecular physical behavior dominates, but at larger distances the wave propagation is governed by solid-state physical rules. The calculations show complex charge-spreading phenomena at graphene grain boundaries. Our results reveal a new picture of charge propagation in graphene, which has important consequences for nanoelectronic applications.

DOI: 10.1103/PhysRevB.85.125443 PACS number(s): 81.05.ue, 68.37.Ef, 73.40.Gk

I. INTRODUCTION

The exponential decrease of physical feature size[1] of bulk silicon-based integrated circuits over time is expected to reach a physical limit in some years.[2] Therefore, developing a semiconductor design paradigm based on alternate materials is necessary in order to make possible the further miniaturization. One of the promising candidates is graphene,[3] a single sheet of graphite. It is a one-atom-thick sheet of sp^2 bonded carbon atoms arranged in a honeycomb lattice. Graphene is different from the semiconductor materials commonly used in microelectronics because it has a linear energy dispersion relation near the Fermi level. The $E(k_x,k_y)$ function is shaped like an inverted pair of cones that meet in a single point—the so-called Dirac point—in momentum space. This photonlike, quasirelativistic behavior gives rise to a variety of phenomena which was not possible to study in condensed matter physics, such as the Klein paradox,[4] Andreev reflection,[5] Veselago lens,[6] etc. This $E \approx E_F$ (near-to-Fermi-energy) behavior of graphene band structure has been extensively studied[7] in recent years theoretically and also experimentally. The peculiar properties of graphene are only now beginning to be understood, and the detailed many-body physics has been shown to be important.[8] Because of the high mobility and long coherence length, the details of many-body interactions and strong coherence over reasonable sizes means that the simple quasiclassical approaches used in most semiconductor devices are not adequate in graphene. Less is known, however, about the high excitation energy range when $E - E_F > 1\,\mathrm{eV}$ (i.e., about the far-from-Fermi-energy domain). It was shown recently[9] that electron beam splitting, collimation, and beam guiding can all be realized by heterodimensional graphene junctions, without applying an external electric field. This is possible in the hot-energy region, where the $E(\vec{k})$ dispersion relation, which is isotropic near the Fermi energy [i.e. $E(\vec{k}) = E(k)$ if $k \approx k_F$] becomes anisotropic if k is far from k_F.

Scanning tunneling microscopy (STM) is one of the main techniques used to investigate with atomic resolution carbon nanostructures[10–12] and devices fabricated from them. Therefore the precise understanding of the STM imaging mechanism (i.e., the current flow from the STM tip to the graphene surface) is important for nanotechnology. An atomically sharp STM tip is a quantum tunneling contact (QTC). Similarly to a quantum point contact (QPC), the electrons can enter from the tip into the sample only through a narrow channel (its width is 0.1–0.2 nm for atomically sharp tips)[13] but contrary to a QPC, no conducting channel exists; electrons can cross the channel only via the tunnel effect. The charge transfer through a QTC is different from that of a QPC both quantitatively and qualitatively. The tunneling probability in an STM experiment is typically $T = 10^{-6}$–10^{-3}, hence the resistance of an STM QTC is several $M\Omega$ instead of the $h/2e^2 = 13\,k\Omega$ minimal value characteristic of a QPC. The few electrons that tunnel are selected so that the transverse momentum and the higher-energy electrons are preferred by the QTC. Moreover, when the STM sample is not a simple metal, the tunneling process includes complicated multiple scattering and interference effects between the tip states and sample states.[14] The outcome of this complex scattering process determines $T(\vec{k})$, the transmission probability as the function of the incoming momentum. Only those few electrons surviving this selection process remain on the sample and can spread on it, reaching the other (ground) STM electrode after a macroscopic spreading. The pattern of this eventual spreading is determined by two factors: i) the band structure of the sample and ii) the pattern of electronic waves remaining on the sample at the end of the initial selection process mentioned above. One can distinguish two spatial regions in an STM tip–sample system: the near and far regions, somewhat similar to the near- and far-field regions distinguished for a radiating electromagnetic antenna. The region that participates at the multiple scattering process between tip and sample is the near region. That region where the influence of the tip is negligible is the far region.

In this paper we examine in detail the dynamics of the STM tunneling process from an atomically sharp STM tip onto the

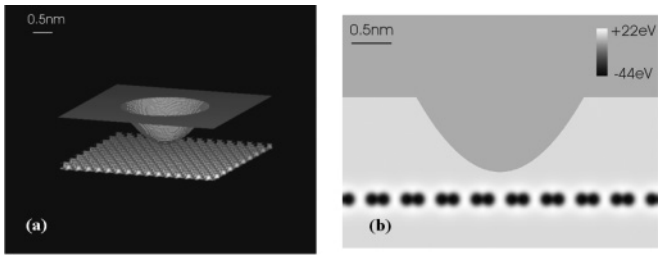

FIG. 1. Model geometry of the STM tip graphene system. (a) −2.7 eV equipotential surface of the potential. The surface is clipped at the boundary of the presentation box. (b) Grayscale image of the 2D cross section of the potential. The hyperbolic protrusion on the upper half plane and the horizontal row of black dots represent the vertical cross sections of the tip and graphene, respectively. Black (white) denotes smallest (largest) potential values. The dark gray level at the upper part is the negative potential inside the STM tip (−9.81 eV), the light gray level at the lower part is the vacuum potential (zero).

graphene surface, both in the near and the far regions. The analysis is performed both in time and energy domain, giving a full picture of the quasiparticle dynamics within the level of the local one-electron pseudopotential model of graphene.

The organization of the paper is as follows. In Sec. II the tunnel barrier is constructed for the STM tip–graphene tunnel junction. Section III gives an outline of the wave-packet dynamical method for calculating the tunnel current and it is explained how the eigenfunctions are calculated from the time-dependent wave function. In Sec. IV numerical results are presented for the energy- and time-dependent probability density distribution and probability current distribution. Section V is devoted to the discussion of the results.

Hartree atomic units are used in all formulas except where explicit units are given. SI units are used, however, in all the figures and numerical data.

II. MODEL POTENTIAL

The model system is shown in Fig. 1. In order to reduce the many-particle problem into a one-particle problem we used a local one-electron pseudopotential[15] matching the *ab initio* band structure of graphene as best as possible. This is a parametrized potential having the following form:

$$V_{\text{graphene}}(\vec{r}) = \sum_{j=1}^{N} \sum_{i=1}^{3} A_i e^{-a_i|\vec{r}-\vec{r}_j|^2} \qquad (1)$$

where $\vec{r}_j$ denote the atomic positions and N is the number of atoms. The A_i, a_i coefficients are given in Ref. 15. The potential forms low-value channels between the nearest-neighbor C atoms and has a large positive value at the centers of the hexagons. This effectively prevents the electron to enter the center region; most of the probability current has to flow along the bonds, as is seen in the wave-packet dynamical simulation during the transient period (Sec. IV B). As shown there at later times in the far region, the probability current still flows along the C-C bonds locally, but the interference of these local currents determine the direction of the propagation of the wave packet.

The STM tip is represented by a jellium background model. The tip is taken as a hyperboloid of 0.5 nm apex radius and 15° aperture angle. The jellium potential is zero outside the effective surface of the tip and −9.81 eV inside (see Ref. 16 for details). While most of the discussion of our calculations is done for the tip apex lying above the center of a hexagon, the effects of the tip position on the spreading pattern are examined in Sec. IV D.

III. CALCULATION METHOD

In our calculation a Gaussian wave packet is injected into the graphene sheet from the simulated metallic STM tip and its time development is calculated by wave packet dynamics. Wave-packet dynamics[17,18] is an effective method to study electron tunneling through nanostructures. Some of its advantages are: it includes all multiple scattering and interference effects, it is well suited for the study of localized systems, it gives insight into the dynamics of the system, it can be effectively parallelized, but it is possible to calculate results for realistic three-dimensional (3D) systems even on a PC. The Gaussian wave packet is launched with the Fermi momentum $\vec{k} = (0,0,-k_F)$ from inside the tip bulk toward the apex of the tip. The width of the wave packet has to be chosen to meet two criteria: i) its energy spread has to extend to the region of interest (which is ±3 eV in our calculation) and ii) its real space width has to be significantly larger than the width of the STM-tip–graphene-tunneling channel. Our chosen value of $\Delta x = \Delta y = \Delta z = 0.37$ nm meets these criteria. This Gaussian is the $\psi_0(\vec{r};t)$ initial condition of the dynamics calculation, where $\vec{r} = \{x,z,y\}$. The $\psi(\vec{r};t)$ time-dependent wave function is computed from the time-dependent 3D Schrödinger equation by the split operator Fourier transform method[19,20] (also called the spectral method). Absorbing boundary conditions are realized by a drain potential around the presentation box.[21] Utilizing a $t \to E$ Fourier transform, the $\psi(\vec{r};E)$ energy-dependent wave function is calculated from the time-dependent wave function. The energy resolution of the $\psi(\vec{r};E)$ wave function can be increased to any desired accuracy by increasing the $T_{\max}$ integration time. A 0.1 eV accuracy was used in our calculation. In order to normalize $\psi(\vec{r};E)$ properly, we repeated the whole calculation for a free particle, $V(\vec{r}) \equiv 0$, then each $\psi_{V\equiv 0}(\vec{r};E)$ function was normalized individually to 1. $N(E)$ normalization coefficients calculated this way were applied to $\psi(\vec{r};E)$. The simulation was carried out using a modified version of our computer code developed for solving the time-dependent Schrödinger equation in the case of supported carbon nanotubes.[16,22,23]

IV. RESULTS

A. Energy-dependent analysis

Figure 2 shows the energy-dependent probability density, $\varrho(\vec{r};E) = |\psi(\vec{r};E)|^2$, for several characteristic energy values. The inset shows $P_{\text{graphene}}(E)$, the energy-dependent probability of finding the quasiparticle on the graphene surface

$$P_{\text{graphene}}(E) = \int_{\text{graphene}} \varrho(\vec{r};E)dV, \qquad (2)$$

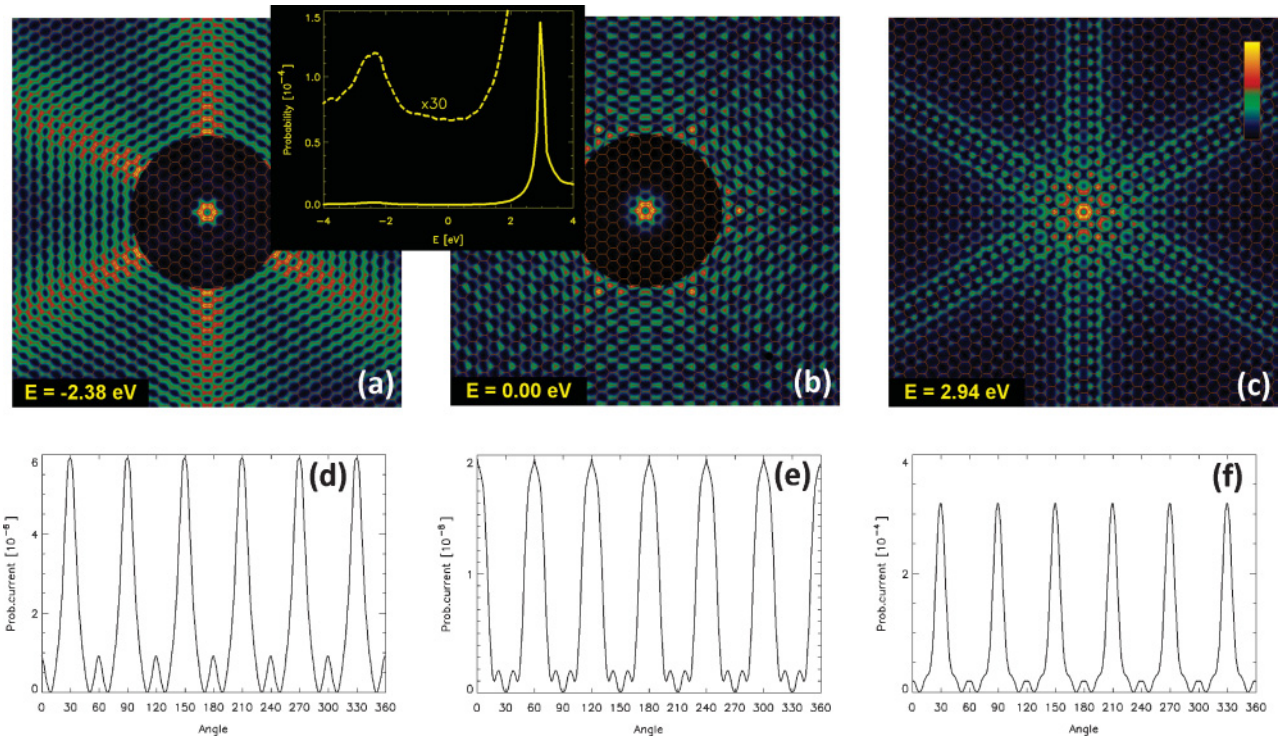

FIG. 2. (Color online) (a)–(c) Probability density on the graphene sheet for selected energies shown as color-coded 2D sections. We used a nonlinear color scale [see the scale bar in (c)]. Black corresponds to zero density, bright yellow to the maximum density. Each subimage is renormalized individually to its maximum density. In (a) and (b) the far region is shown on a separate (enhanced) color scale. Maximum density values are 2.33×10^{-3} (2.58×10^{-5}), 1.94×10^{-3} (3.60×10^{-7}), 4.52×10^{-3} (1.15×10^{-3}) for the near (far) regions of (a), (b), and (c), respectively. Probability density values are relative to that measured in the tip bulk. The graphene network is shown by thin orange lines. Size of the presentation window is 7.68 nm. The inset shows the *P(E)* probability on the graphene. (d)–(f) Angular distribution of the probability current for the three energy values shown in (a)–(c) in the far region. Magnitude is relative to the incoming probability current at that energy.

where the integration is done for a volume including the graphene sheet, taken sufficiently thick that the eigenfunctions decrease to a negligible value at the upper and lower boundaries. The total tip-graphene–tunneling probability is $T(E) = P_{\text{graphene}}(E) + P_{\text{clipped}}(E)$, where $P_{\text{clipped}}(E)$ is the probability for that region of the graphene that is outside the presentation window, where the absorbing boundary condition is in effect. According to our calculations this is a small quantity, hence $T(E) \approx P_{\text{graphene}}(E)$. As shown in Fig. 2 (inset), there are two peaks at $P_{\text{graphene}}(E)$: a small peak at $E_{\text{lo}} = -2.38$ eV and a large peak at $E_{\text{hi}} = 2.94$ eV (energies are relative to the -5 eV Fermi energy). Figures 2(a)–2(c) display the $\varrho(\vec{r}; E)$ probability density for these three characteristic energy values: E_{lo}, E_F, and E_{hi}. The peaks of $P_{\text{graphene}}(E)$ at E_{lo} and E_{hi} correspond to the peaks of the density of states (DOS) of graphene at $E = E_F \pm \gamma$ where $\gamma = 2.6$ eV is the tight-binding C-C hopping matrix element. The peaks of $P_{\text{graphene}}(E)$ at E_{lo} and E_{hi} are shifted with an amount of $\Delta E = 0.3$ eV towards higher energies from the DOS peak positions. This is caused by the exponential energy dependence of the tunnel effect, which shifts the peaks toward higher energies. This same exponential dependence explains the ratio of the two peaks: $P_{\text{graphene}}(E_{\text{lo}}) \ll P_{\text{graphene}}(E_{\text{hi}})$. Let us now turn our attention to the shape of the $\varrho(\vec{r}; E_{\text{lo}})$, $\varrho(\vec{r}; E_{\text{hi}})$ functions. The $\varrho(\vec{r}; E_{\text{lo}})$ and $\varrho(\vec{r}; E_{\text{hi}})$ probability density functions [Figs. 2(a),2(c)] are anisotropic, higher intensities are seen in the six zigzag directions. This corresponds to the 6 ΓK directions in the Brillouin zone of the graphene sheet. Indeed, the $E(\vec{k}) = E$ isoenergy curves in momentum space are warped into hexagons, when E is far from E_F, which makes the v_g group velocity have a sixfold symmetry. Trigonal warping[24] becomes enhanced, when $E - E_F \approx \gamma$. Zigzag spreading is also seen on the angular probability current plots shown in Figs. 2(d) and 2(e).

Figures 2(b) (2(e)) display the probability distribution (probability current distribution) near the Fermi energy, respectively. These functions have two important characteristics: i) their magnitude in the far region is considerably smaller (cf. the numbers in the caption of Fig. 2) than that seen on E_{lo} and E_{hi}, and ii) both functions show an anisotropic spreading at E_F. The small values of $\varrho_{\text{far}}(\vec{r}; E_F)$ and $\vec{j}_{\text{far}}(\vec{r}; E_F)$ are easily explained by taking into account the vanishing DOS of graphene at E_F. The anisotropic spreading, however, seems surprising, because the isoenergy curves $E(\vec{k}) = E$ are circles around E_F and also the incoming wave packet has a cylindrical symmetry.

B. Time-dependent analysis

In order to understand this peculiar anisotropic spreading around E_F, we performed a detailed investigation of the dynamics of the transient period, which begins when the WP tunnels from the STM tip onto the graphene surface and lasts

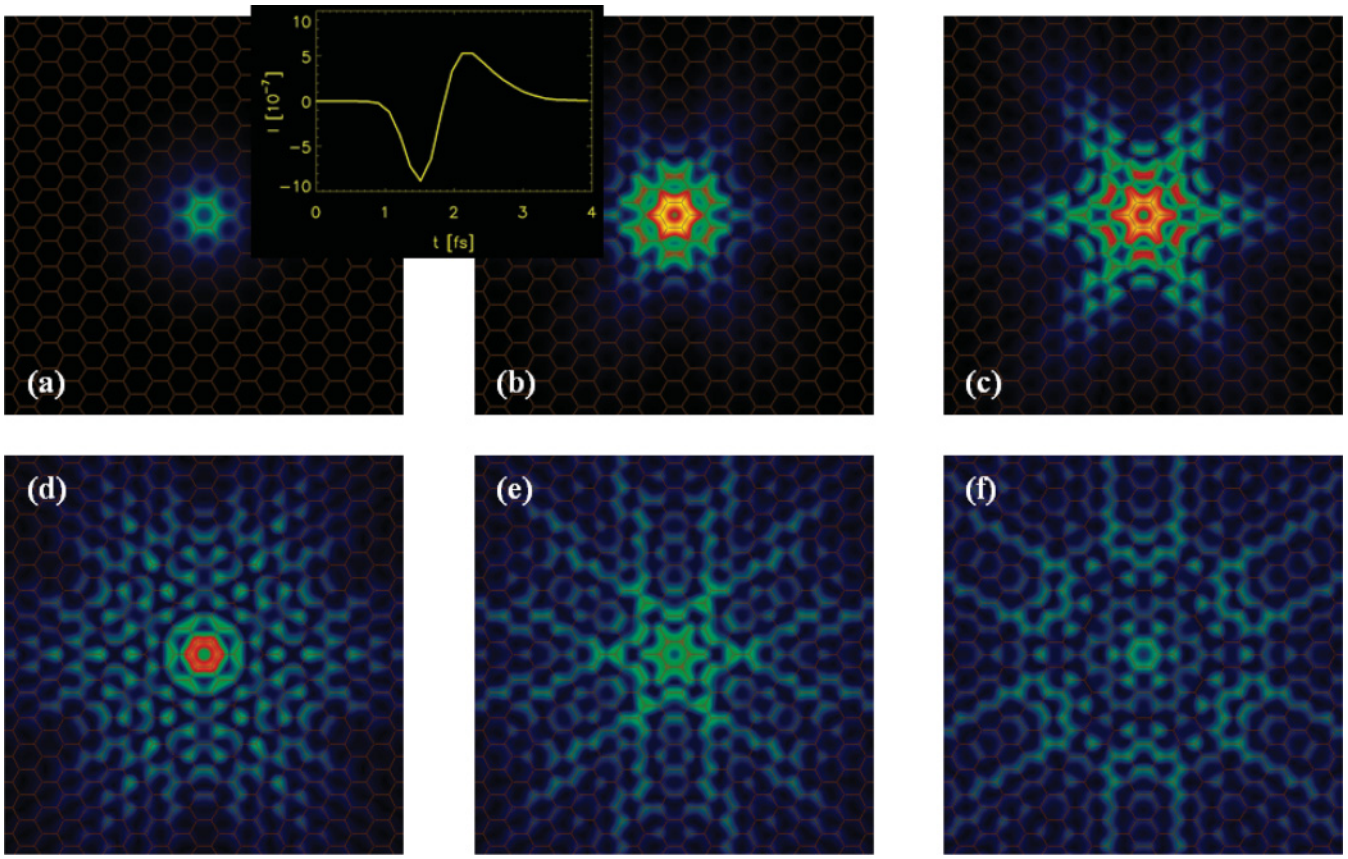

FIG. 3. (Color online) Selected snapshots from the time evolution of the probability density of wave packet shown as color-coded 2D sections. Black corresponds to zero probability. We used the same color scale on all images, determined by the maximum probability density on the graphene sheet. The graphene network is shown by thin orange lines. Time values are: 1.22 fs, 2.00 fs, 2.45 fs, 3.14 fs, 3.52 fs, 4.19 fs. See the text for details. Size of the presentation window is 3.84 nm in both x and y directions. The inset shows the probability current $I(t)$ flowing from the tip into the graphene surface.

until the stable, far region spreading pattern is formed. Figure 3 shows the details of the time evolution of the wave packet. Only the middle part (3.84×3.84 nm^2) of the presentation window is shown, in order to facilitate investigation of the near region (see the movies in the Supplementary Material).[25] As the wave packet reaches the tip apex from inside the tip bulk, it begins to tunnel onto the central hexagon (i.e., that below the tip apex, $t = 1.22$ fs). Then the wave packet begins to spread on the graphene sheet along the C-C bonds, following the hexagonal symmetry ($t = 2.00$ fs, $t = 2.45$ fs). At $t = 3.14$ fs, after spreading 1.2 nm from the center, the direction of the spreading is changed. Further spreading ($t = 3.52$ fs, 4.19 fs) occurs along the 6 ΓK directions of the Brillouin zone, which matches the zigzag direction of the graphene sheet in direct space. As we saw above, this zigzag spreading is dominated by states of $E = E_{\rm hi} = E_F + 2.94$ eV, because of the DOS peak at $E = E_F + \gamma$. As we can see in Fig. 3, for about two and a half femtoseconds majority of the WP is residing on the few central hexagons of the graphene lattice. This is the very time interval, however, as clearly shown on the inset of Fig. 3, during which a part of the WP tunnels from the tip into the graphene sheet [see the large negative peak at $I(t)$] then the majority of this part tunnels back into the tip [see the large positive peak at $I(t)$]. Only a small fraction, 3.8% of the WP that originally tunneled onto the graphene remains on the graphene surface; the total tunneling probability (weighted energy sum for the Gaussian WP) is 6.8×10^{-7}. During this back-and-forth tunneling, however, a momentum selection process takes place.

C. Small graphene clusters

Electronic states of the sample determine which WP components remain on the graphene and which components tunnel back into the tip. During the transient period, however, the WP does not sample the whole graphene surface, because it spreads only a few hexagons away from the central hexagon over which the STM tip is placed. Hence, in order to determine those electronic states relevant for the selection process we have to study the electronic structure of special graphene clusters composed only of a few hexagons. These graphene clusters are similar to polycyclic aromatic hydrocarbon (PAH) clusters,[26–28] but are special because in real PAH molecules the potential of the edge atoms is different from that of the inner atoms. In our special graphene clusters the same potential was applied to each atom, because in our case all atoms are the same: an sp^2 atom of the graphene surface, just the WP samples different regions of that surface. In other words, these

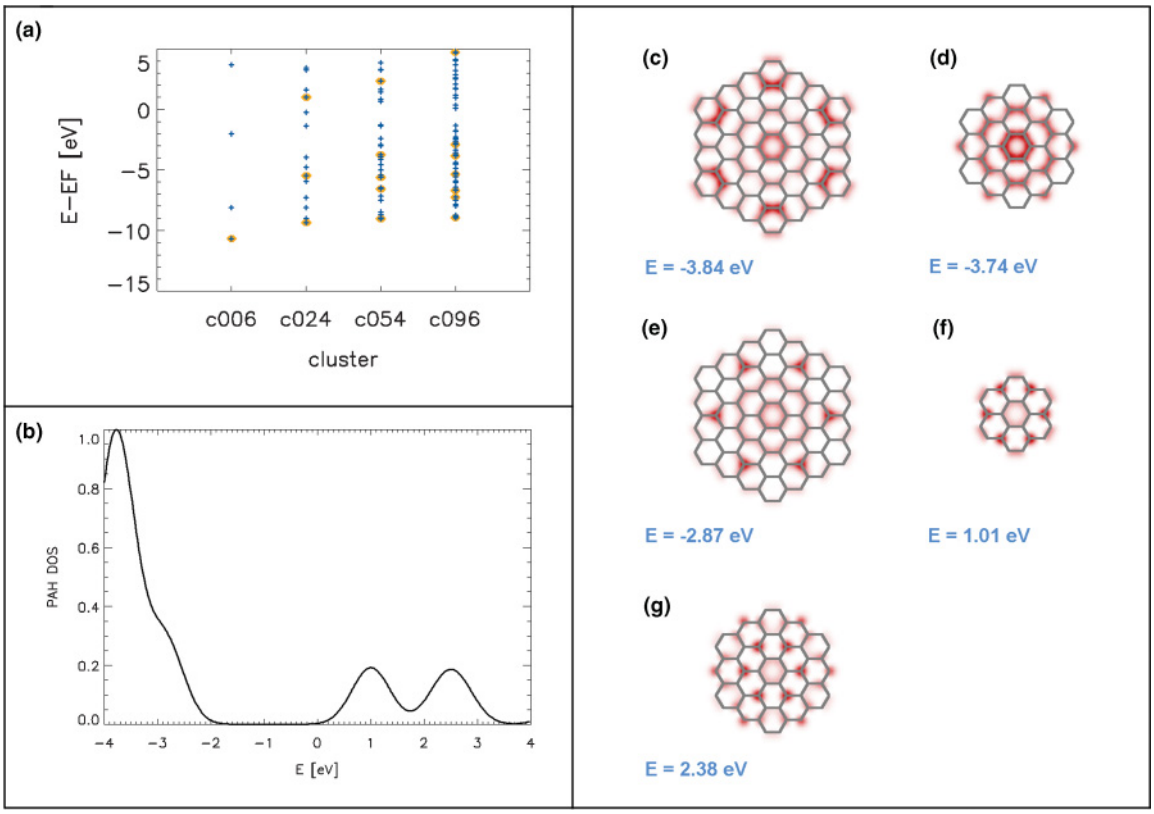

FIG. 4. (Color online) Frozen-and-cut C_{6m^2} graphene clusters (see the text for details). (a) Energy level diagram. Those states with hexagonal symmetry are shown by large yellow circles. (b) Tunneling density of states for all PAH-like states with hexagonal symmetry in the $[-4,+4]$ eV window. A broadening of 0.5 eV was applied, because of the small lifetime of these states. (c)–(g) Probability density for those states with hexagonal symmetry in the $[-4,+4]$ eV window.

clusters are frozen and cut from the infinite graphene surface. Tip perturbation on the electronic states of the sample[29,30] can be neglected, when the tip is far enough. We have calculated the $\psi^{\rm PAH}_{m,n}(\vec{r})$ orbitals and $E^{\rm PAH}_{m,n}$ energies of small PAHs of formula C_{6m^2} ($m = 1,2,3,4$), where n is the quantum number. These are frozen-and-cut graphene clusters, as explained above, all bond lengths were fixed to 0.142 nm. Figure 4(a) shows the $E^{\rm PAH}_{m,n}$ energies thus calculated. Deretzis *et al.* calculated[31] the electronic structure and geometry of small PAH molecules using different methods. As a reference they used a DFT calculation, then considered several levels of semiempirical methods, ending with a simple tight binding (TB). Figure 2 of Ref. 31 shows the HOMO-LUMO gap obtained from the different methods. HOMO-LUMO gaps calculated from our $E^{\rm PAH}_{m,n}$ levels are very close to the TB results of Ref. 31. This is natural because in simple TB Deretzis *et al.* used the same C-C matrix element for all atoms, which is similar to our frozen-and-cut graphene clusters. Next we calculated the $c^{\rm PAH}_{m,n} = \langle\psi^{\rm PAH}_{m,n}(\vec{r})|\psi_{\rm tip}(\vec{r})\rangle$ matrix elements, where $\psi_{\rm tip}(\vec{r})$ is the tip wave function. These matrix elements tell us, within the first level of perturbation theory, which PAH-like states are excited and with what (complex) amplitude.

The most important selection criterion is, of course, the symmetry. $\psi_{\rm tip}(\vec{r})$ being a Gaussian, has a cylindrical symmetry around a vertical (z direction) line crossing the graphene plane at the center of a hexagon because the tip is situated above the center of a hexagon. This rules out all $\psi^{\rm PAH}_{m,n}(\vec{r})$ orbitals with no hexagonal symmetry; for example all states with (vertical) mirror planes are canceled [e.g., those, where $\psi^{\rm PAH}_{m,n}(x,y,z) = \psi^{\rm PAH}_{m,n}(-x,y,z)$]. Figure 4 shows an overview of the bound states for our small graphene clusters. The energy level diagram of all states is displayed in Fig. 4(a). Those states with hexagonal symmetry (nonzero matrix element) are marked with large yellow circles. As it is shown in Ref. 28, C_{6m^2} clusters do not have states at E_F. There are several states, however, in the [–4 eV, +4 eV] energy window of our WP calculation. These levels are shown in Fig. 4(b), weighted with the matrix element. A broadening of $\Delta E = 0.5$ eV was applied, because of the small (≈ 1 fs) lifetime of these states. Figures 4(c)–4(g) show the $|\psi^{\rm PAH}_{m,n}(\vec{r})|^2$ probability density for the hexagonal cluster states. These states are excited by the incoming wave packet during the transient period and the time-dependent superposition of these states forms the time-dependent patterns seen on the WP dynamical calculation at the near region (cf. Fig. 3). After the transient period, quasiparticles concentrated on the PAH-like states spread out to the whole graphene surface. This explains the hexagonal anisotropy seen in the spreading even at E_F (cf. Fig. 2): The PAH-like states are all hexagonal and since they filter out the initial states for the spreading into the far region, the hexagonal anisotropy is preserved for the whole process.

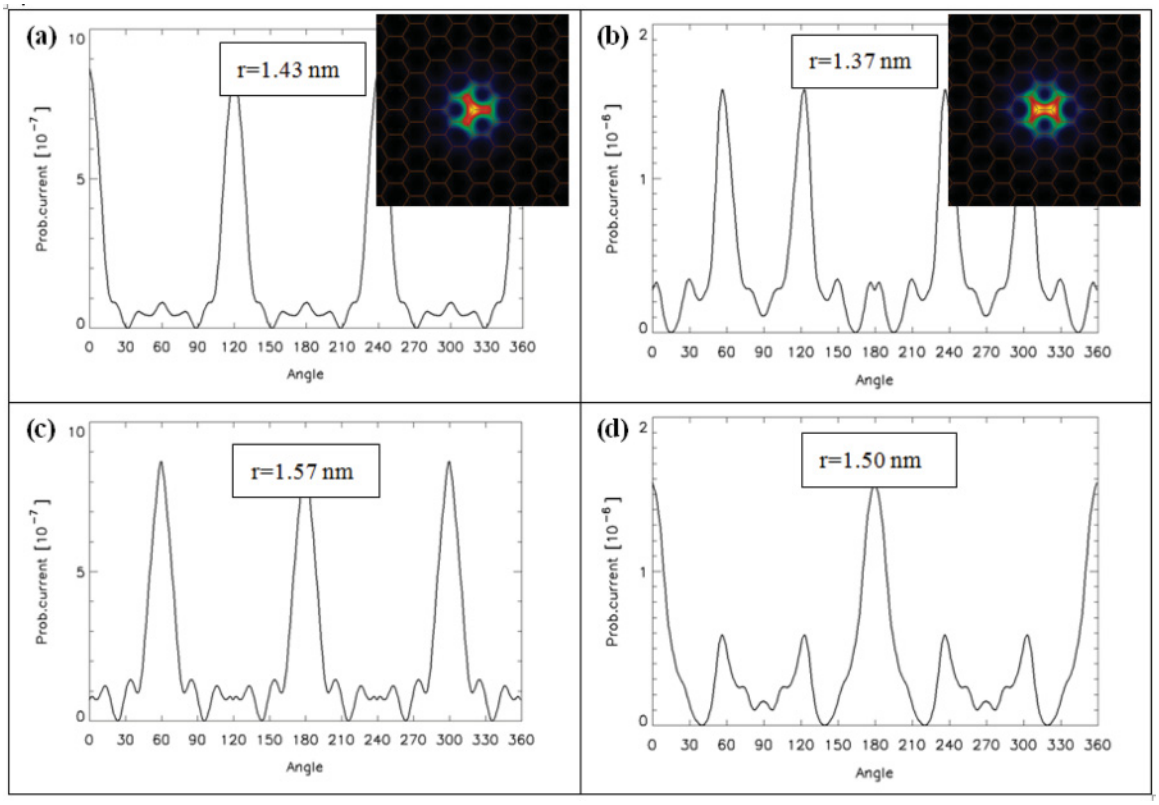

FIG. 5. (Color online) Angular distribution of the probability current density near the Fermi energy in the far region for different tip positions and different radial distances. (a), (c): Tip above an atom. (b), (d): Tip above the center of a C-C bond. The insets show the probability density distribution in the near region for the two tip positions.

The situation is similar to that observed in quantum point contact experiments,[32] where two large electron reservoirs possessing many states are connected through a narrow channel, which has only a small number of conducting channels. This system has a nonzero resistance even in case of no impurities, because reflections occur when a small number of propagating modes in the waveguide is matched to a large number of modes in the reservoirs. In our case the STM tip and the infinite graphene surface are the two reservoirs, but the conduction can only proceed through small integer number of states of the small graphene clusters during the transient period.

D. Effect of the tip position

The STM tip had a very special, symmetrical position in the calculations studied so far: The tip was placed above the center of a hexagon of the graphene surface. In this section we investigate the effect of the tip position: which of our conclusions are specific to the hexagonally symmetric tip position and which are independent of the tip position? In order to clarify these questions we performed WP dynamical simulations for different tip positions: when the tip is above an atom and when it is above the center of a C-C bond. In this paper only the main results, which answer the above question concerning the robustness of our results above, are presented. Details of these calculations will be published elsewhere. Figure 5 shows the $\varrho_{\rm near}(\vec{r};E_F)$ probability density distributions in the near field and the $\vec{j}_{\rm far}(\vec{r};E_F)$ probability current density distributions in the far field for the two tip positions: tip above the atom and above the C-C bond. The $\varrho_{\rm near}(\vec{r};E_F)$ functions inherit the symmetry of the initial state, threefold in the above the atom and twofold in the above the bond configurations. This is because the $c^{\rm PAH}_{m,n}=\langle\psi^{\rm PAH}_{m,n}(\vec{r})|\psi_{\rm tip}(\vec{r})\rangle$ matrix elements (Sec. IV C) are now nonzero for threefold and twofold symmetric $\psi^{\rm PAH}_{m,n}(\vec{r})$ functions. Comparing the $\vec{j}_{\rm far}(\vec{r};E_F)$ functions with those for the above the hexagon configuration (Fig. 2) note that the magnitude of the current is larger by one or two orders of magnitude. Calculations in Ref. 28 show that threefold and twofold symmetric small PAHs do have states at the Fermi energy. Hence those components of the incoming WP with $E=E_F$ find acceptor states on the small graphene clusters and so these are not tunneling back into the tip, but spread into the far region. Observe now the angular distribution of the $\vec{j}_{\rm far}(\vec{r};E_F)$ functions, shown in Figs. 5(a), 5(c) [5(b), 5(d)] for the threefold (twofold) symmetric tip positions. A background armchair sixfold symmetry is present in all the angular distributions but the symmetry of the initial state (threefold and twofold) is also present. In the case of the above the atom (above the bond) configuration two threefold (twofold) symmetric configurations alternate periodically with increasing radius. As a result, a global sixfold symmetry is present in $\vec{j}_{\rm far}(\vec{r};E_F)$ for all the three tip positions studied, hence it is not a consequence of the symmetry of the initial condition but a consequence of the sixfold symmetric graphene lattice.

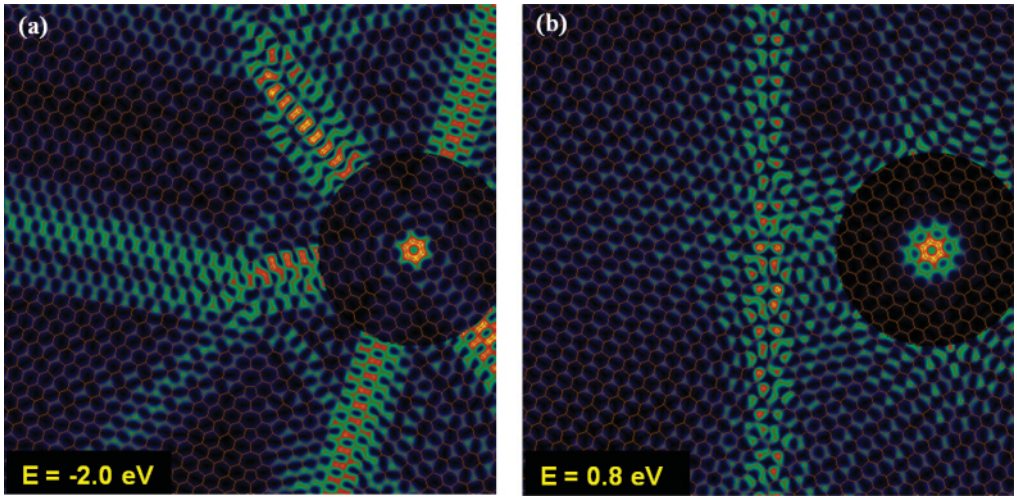

FIG. 6. (Color online) Probability density on the graphene sheet with the grain boundary for selected energies shown as color-coded 2D sections. Black corresponds to zero density, bright yellow to the maximum density. The far region is shown on a separate (enhanced) color scale. The graphene network is shown by thin orange lines. Size of the presentation window is 7.68 nm.

V. DISCUSSION

Figures 3 and 5 show the scattering of an axially symmetric wave packet by a graphene sheet. This process is perturbed in the near region by the tip that is used to launch the wave. It is indeed true that the problem bears resemblance with the scattering of a Bloch wave by a defect, leading to interferences that may construct a complicate standing wave pattern. The analogy cannot be pushed too far, however, because the dynamics is much more complex in the present context than it is in a stationary problem. In addition, the incident wave packet is not an eigenstate of perfect graphene. The near region filters out those components of the incoming wave packet that match the spectrum of a small cluster receptor according to selection rules imposed by the symmetry of the tip-graphene system. While those components spread away in the far region, the others are reflected back to the tip. When the tip is localized above a hexagon center of graphene, there is a nice collimation of beams along six branches in the far region. The pattern is not that simple for less symmetric geometries. The tip is indeed a defect that may be moved at will.

We now turn to discuss some experimental implications of our results. It should be possible to detect an anisotropic differential resistance with sixfold symmetry in low-temperature transport experiments on graphene, where one of the electrodes is a sharp localized probe. In conventional transport experiments we do not have a tunneling situation, it is more like many superimposed point contacts. The point contacts behave differently[22] as compared to a pure tunneling situation. While a tunnel contact strongly selects those tip states with momentum perpendicular to the graphene surface, the angular dependence of the transmission is much wider[22] for a point contact. As graphene is a zero gap semiconductor, under the widely used experimental conditions, when large contact area electrodes are used, and the angle of incidence of the wave packets on the interface can vary over a certain range, lower energy spreading states are likely to tunnel, too. An anisotropic conductivity may also appear in conventional transport experiments, however, at energies close to the Fermi energy, because the effect of short-range nonsymmetric defects[33] or because the Rashba spin-orbit coupling[34] caused by impurities[35] or by the interaction with the support surface.[36]

A very important factor that may affect the propagation of charge carriers[37,38] in graphene is the presence of grain boundaries. From the point of view of electronic applications it is important to note that the charge carrier mobility of CVD-grown graphene can be orders of magnitude smaller[39] than that reported for cleaved graphene.[40,41] CVD graphene is a patchwork of large-angle grain boundaries[42,43] with sizes in the 100 nm range. Figure 6 shows the energy-dependent probability density, $\varrho(\vec{r}; E)$, calculated for a grain boundary for two characteristic energy values. The 38.9° grain boundary[44] is a linear chain of abutting pentagons and heptagons separated by one row of hexagons, relaxed by a molecular mechanics potential. The simulated STM tip is on the right side. Our calculations show a rich variety of transport phenomena, including beam splitting [Fig. 6(a)] and states localized on the grain boundary [Fig. 6(b)]. The $\varrho(\vec{r}; E)$ probability density at $E = 0.8$ eV is indeed similar to the simulated STM image calculated by Yazyev and Louie [see LAGB I in Fig. 5(c) of Ref. 31]. The $E = 0.8$ eV energy of the localized state corresponds to a DOS peak at $E = 0.5$ eV if we take into account the $\Delta E = 0.3$ eV shift introduced in Sec. IV A. Details of the wave-packet transport calculation for the grain boundary are outside the scope of this paper, but the preliminary results presented here clearly prove the value of wave-packet transport calculations for complicated graphene junctions.

VI. CONCLUSION

In summary, our simulations show that when tunneling from an atomically sharp STM tip into the graphene surface, there is a transient period of $\Delta t \approx 3$ fs duration. The wave packet needs this time to decide how to spread on the graphene sheet. The tunneling from the tip into the graphene surface proceeds in two steps. First, a portion of the wave packet tunnels onto

the graphene surface, then a majority of it tunnels back into the tip. Only those portions remaining on the graphene can spread into the far region. The situation is similar to that analyzed by Landauer:[45] Electrons coming from a large reservoir (tip) can access the another large reservoir (graphene surface) only through a system having only a few states (small graphene clusters). The small graphene clusters select specific states from the incoming wave packet. The selection is influenced by the symmetry of the tip position relative to the graphene surface, but an anisotropic, sixfold symmetric pattern caused by the sixfold symmetry of the graphene lattice is always present in the spreading when utilizing an atomically sharp tip. Symmetry of the lattice has such a considerable effect on the spreading, because the Fermi wavelength in graphene ($\lambda_F = 0.74$ nm)[46] is comparable to the lattice constant. By a detailed study of the time-dependent dynamics of wave packets on graphene sheets it is possible to identify the boundary between the molecular physical and solid-state physical description of the graphene sheet. At small distances the molecular physical behavior dominates, but at larger distances the solid-state physical picture takes over. Utilizing these anisotropic conduction effects, by patterning the graphene sheet[47] into specific ribbons and junctions it is potentially possible to build all-carbon nanoelectronic circuits, possibly using geometries reported earlier.[9] Our simulations show that in the regions in which an accumulation of structural defects is found—like in grain boundaries in CVD graphene—the charge-spreading phenomena are dramatically altered. Further, more detailed work is needed to reveal in full the phenomena to be expected in such regions.

ACKNOWLEDGMENTS

This work has been conducted within the framework of the Joint Korean-Hungarian Laboratory for Nanosciences (JKHLN), the Converging Research Center Program through the Ministry of Education, Science and Technology (2010K000980) and the OTKA-NKTH, Grant No. 101599 in Hungary. G.I.M. and L.P.B. gratefully acknowledge a grant from the Belgian Fonds de la Recherche Scientifiques (FNRS). Helpful discussions with Alex Mayer of FUNDP, Namur, are gratefully acknowledged.

*mark@sunserv.kfki.hu; www.nanotechnology.hu

[1] G. E. Moore, Electronics **38** (1965).
[2] [http://public.itrs.net].
[3] K. S. Novoselov, A. K. Geim, S. V. Morozov, D. Jiang, S. V. Dubonos, I. V. Girgorieva, and A. A. Firsov, Science **306**, 666 (2004).
[4] O. Klein, Z. Phys. **53**, 157 (1929).
[5] A. F. Andreev, Sov. Phys. JETP **19**, 1228 (1964).
[6] V. G. Veselago, Sov. Phys. Usp. **10**, 509 (1968).
[7] C. W. J. Beenakker, Rev. Mod. Phys. **80**, 1337 (2008).
[8] Y. Barlas, T. Pereg-Barnea, M. Polini, R. Asgari, and A. H. MacDonald, Phys. Rev. Lett. **98**, 236601 (2007).
[9] Z. Wang and F. Liu, ACS Nano **4**, 2459 (2010).
[10] L. P. Biró and P. Lambin, *Scanning Tunneling Microscopy of Carbon Nanotubes* (American Scientific Publishers, Fairfield, New Jersey, 2003), pp. 1–12.
[11] Y. Kobayashi, K. I. Fukui, T. Enoki, K. Kusakabe, and Y. Kaburagi, Phys. Rev. B **71**, 193406 (2005).
[12] P. Lauffer, K. V. Emtsev, R. Graupner, T. Seyller, L. Ley, S. A. Reshanov, and H. B. Weber, Phys. Rev. B **77**, 155426 (2008).
[13] A. A. Lucas, H. Morawitz, G. R. Henry, J.-P. Vigneron, P. Lambin, P. H. Cutler, and T. E. Feuchtwang, Phys. Rev. B **37**, 10708 (1988).
[14] K. K. Saha, J. Henk, A. Ernst, and P. Bruno, Phys. Rev. B **77**, 085427 (2008).
[15] A. Mayer, Carbon **42**, 2057 (2004).
[16] G. I. Márk, L. P. Biró, and J. Gyulai, Phys. Rev. B **58**, 12645 (1998).
[17] B. M. Garraway and K.-A. Suominen, Rep. Prog. Phys. **58**, 365 (1995).
[18] G. Varga, J. Phys.: Condens. Matter **14**, 6081 (2002).
[19] J. A. Fleck, J. R. Morris, and M. D. Feit, Appl. Phys. **10**, 129 (1976).
[20] M. D. Feit, J. A. Fleck, and A. Steiger, J. Comput. Phys. **47**, 412 (1982).
[21] B. Poirier and T. C. Jr., J. Chem. Phys. **118**, 17 (2003).
[22] G. I. Márk, L. P. Biró, J. Gyulai, P. A. Thiry, A. A. Lucas, and P. Lambin, Phys. Rev. B **62**, 2797 (2000).
[23] G. I. Márk, L. P. Biró, and P. Lambin, Phys. Rev. B **70**, 115423 (2004).
[24] R. Saito, G. Dresselhaus, and M. S. Dresselhaus, Phys. Rev. B **61**, 2981 (2000).
[25] See Supplemental Material at http://link.aps.org/supplemental/10.1103/PhysRevB.85.125443 for two AVI movies showing the time development of the probability density of a wave packet when the STM tip is above an atom and when it is above the center of a hexagon.
[26] W. E. Moffitt and C. A. Coulson, Proc. Phys. Soc. **60**, 309 (1948).
[27] M. R. Philpott and Y. Kawazoe, J. Chem. Phys. **131**, 214706 (2009).
[28] M. Ezawa, Phys. Rev. B **76**, 245415 (2007).
[29] E. Tekman and S. Ciraci, Phys. Rev. B **40**, 10286 (1989).
[30] L. Tapasztó, G. I. Márk, A. A. Koós, P. Lambin, and L. P. Biró, J. Phys.: Condens. Matter **18**, 5793 (2006).
[31] I. Deretzis, G. Forte, A. Grassi, A. L. Magna, G. Piccitto, and R. Pucci, J. Phys.: Condens. Matter **22**, 095504 (2010).
[32] C. W. J. Beenakker and H. van Houten, Solid Stat. Phys. **44**, 1 (1991).
[33] F. T. Vasko, Appl. Phys. Lett. **96**, 212103 (2010).
[34] I. Gierz, J. Dil, F. Meier, B. Slomski, J. Osterwalder, J. Henk, R. Winkler, C. Ast, and K. Kern, e-print arXiv:1004.1573.
[35] A. H. CastroNeto and F. Guinea, Phys. Rev. Lett. **103**, 026804 (2009).
[36] P. Rakyta, A. Kormányos, and J. Cserti, Phys. Rev. B **82**, 113405 (2010).
[37] O. V. Yazyev and S. G. Louie, Nature Mater. **9**, 806 (2010).
[38] D. Gunlycke and C. T. White, Phys. Rev. Lett. **106**, 136806 (2011).
[39] X. Li, W. Cai, J. An, S. Kim, J. Nah, D. Yang, R. Piner, A. Velamakanni, I. Jung, E. Tutuc *et al.*, Science **324**, 1312 (2009).
[40] X. Du, I. Skachko, A. Baker, and E. Y. Andrei, Nature Nanotechnol. **3**, 491 (2008).

[41]K. Bolotin, K. Sikes, Z. Jiang, M. Klima, G. Fudenberg, J. Hone, P. Kim, and H. Stormer, Solid State Commun. **146**, 351 (2008).

[42]K. Kim, Z. Lee, W. Regan, C. Kisielowsk, M. F. Crommie, and A. Zettl, ACS Nano **5**, 2142 (2011).

[43]P. Nemes-Incze, K. J. Yoo, L. Tapasztó, G. Dobrik, J. Lábár, Z. E. Horváth, C. Hwang, and L. P. Biró, Appl. Phys. Lett. **99**, 023104 (2011).

[44]P. Simonis, C. Goffaux, P. A. Thiry, L. P. Biró, P. Lambin, and V. Meunier, Surf. Sci. **511**, 319 (2002).

[45]R. Landauer, IBM J. Res. Dev. **1**, 223 (1957).

[46]L. C. Venema, J. W. G. Wildöer, J. W. Janssen, S. J. Tans, H. L. J. T. Tuinstra, L. P. Kouwenhoven, and C. Dekker, Science **283**, 52 (1999).

[47]L. Tapasztó, G. Dobrik,, P. Lambin, and L. P. Biró, Nature Nanotechnol. **3**, 397 (2008).